Chiral quark-meson coupling models for finite nuclei and their (*e*, *e′p*) reactions

Soonchul Choi,[1,2] Tsuyoshi Miyatsu ●,[3] Youngshin Kwon ●,[4,*] Kyungsik Kim,[5,†] Myung-Ki Cheoun ●,[1] and Koichi Saito[3]

[1]*Department of Physics and OMEG Institute, Soongsil University, Seoul 06978, Republic of Korea*
[2]*Center for Exotic Nuclear Studies, Institute for Basic Science (IBS), Daejeon 34126, Republic of Korea*
[3]*Department of Physics, Faculty of Science and Technology, Tokyo University of Science, Noda 278-8510, Japan*
[4]*Research Institute of Basic Science, Korea Aerospace University, Goyang 10540, Republic of Korea*
[5]*School of Liberal Arts and Sciences, Korea Aerospace University, Goyang 10540, Republic of Korea*

The chiral quark-meson coupling (CQMC) models are applied to revisiting static properties of spherical nuclei in comparison with the results from the conventional quantum hadrodynamics (QHD)-like models as well as the available experimental data. They are also used to describe the nuclei off which the electrons scatter to understand their dynamic properties. After calibrating the model parameters at equilibrium nuclear matter density, binding energies, charge radii, single-particle spectra, and density distributions of the nuclei are analyzed and compared. The nonlinear scalar self-interaction in each model is also discussed in consideration of the reproduction of nuclear saturation properties.

I. INTRODUCTION

Ever since J. D. Walecka introduced his namesake model [1], so-called quantum hadrodynamics (QHD) has been established as a relativistic framework for describing nuclear many-body systems with hadronic degrees of freedom. In the original Walecka model, the pointlike nucleons interact through the exchange of Lorentz scalar (σ) and vector (ω) mesons: the former for intermediate-range attraction and the latter for short-range repulsion. The QHD-type models can be practically solved in the mean field approximation, where the meson field operators are replaced with classical fields, and in particular with their ground state expectation values. The phenomenology of nuclear matter and finite nuclei has been studied in QHD with successful results [2–7].

However, it is difficult to describe many-nucleon systems directly from the first principles of quantum chromodynamics (QCD) because of the nonlinear complexity in the low energy regime, although lattice calculations based upon first principles have been being developed with the advent of high-performance computers. Chiral effective field theory (χEFT) that complements such complexity with the idea of scale separation is sophisticatedly applicable to the low energy processes. Thus the so-called *ab initio* methods, e.g., no-core shell model [8,9], Green's function Monte Carlo [10,11], coupled cluster [12,13], in-medium similarity renormalization group [14,15] method, etc., are typically based on the nuclear force described in χEFT. While χEFT is a theory in terms of an expansion in a momentum scale to control the higher dimensional operators of hadronic fields, QHD is

not a consistent effective field theory of QCD but is based on the one-boson exchange picture. The large strength of the meson fields in QHD has motivated somewhat an extension incorporating aspects of QCD.

The quark-meson coupling (QMC) model, the idea of which was first proposed by Guichon [16], is one of the prominent extensions of QHD to consider the effect of the internal quark structure of a nucleon. In the QMC model, the nucleon in nuclear medium is described to be a nonoverlapping MIT bag in which quarks interact with the scalar and vector fields. It is incorporated that the strong scalar field leads to dynamical effects on the internal structure, changing the quark masses inside the nucleon. It was shown that the QMC model describes the saturation properties of infinite nuclear matter [17] and reproduces the properties of finite nuclei [18,19]. It has also been used in the calculation of electron-nucleus scattering cross section to extract the electromagnetic form factors [20]. But it could conflict with the usage of the MIT bag, because the axial charge in the bag is not conserved, and the divergence of the axial vector current does not vanish. The reflection at the bag boundary makes the Lagrangian density of the MIT bag model notinvariant under the global chiral transformation.

An improvement of the QMC model, often referred to as chiral quark-meson coupling (CQMC) model [21], is to take into account spin-dependent structures in the baryon mass spectrum. The hyperfine interaction between light quarks is formed of gluon and pion exchange components with conventional strength. In the CQMC model, the cloudy bag replaces the MIT bag due to the importance of chiral symmetry in the low-energy QCD. The source of axial current at the surface of the bag could act as a source of the pion field, which is converted into the volume-coupling version of the cloudy bag model with the Weinberg transformation. This guarantees the axial vector current to be conserved in

*Corresponding author: ykwon@kau.ac.kr
†Corresponding author: kyungsik@kau.ac.kr

chiral limit. The CQMC model was applied to the equation of state (EoS) for a neutron star in the relativistic Hartree (RH) approximation [22], and also in relativistic Hartree-Fock (RHF) approximation [23–25]. It is demonstrated that, even in the RH approximation, the CQMC perspective improves the calculated mass of the neutron star to the observational constraint, $(1.97 \pm 0.04)M_\odot$ [26–28], in comparison with the QMC result. But the CQMC model has not yet been tested for finite nuclei, nor for their nuclear reactions.

In the present work, the CQMC model in the RH approximation is applied to stable nuclei (from ^{16}O to ^{208}Pb), revisiting their ground-state properties. With the nucleus wave function generated in it, the calculation of knock-out $(e, e'p)$ reactions is implemented so as to study their dynamical effects. For comparison, we employ the QHD and QMC models with and without the nonlinear scalar self-interaction, which is required for an adequate description of the surface properties. Throughout this paper each model without the nonlinear scalar interaction is labeled with 1 (i.e., QHD1, QMC1, and CQMC1), and the models with the nonlinear scalar self-interaction are QHD2, QMC2, and CQMC2. It is interesting to know if and how the model difference is reflected in the calculation of the static and dynamic properties of finite nuclei. It may hardly affect the bulk properties because the parameter sets of the models are determined to reproduce the nuclear properties at saturation point and the finite nuclei are nuclear systems at near-saturation densities. Nonetheless, distinct difference between the models could arise in the estimate of the single-particle energy levels. They can be compared to the cross section data of the one-proton knock-out reactions because the theoretically calculated cross section of them should be dependent on the single-proton energy levels in the nucleus. We also present the results of neutron star properties calculated in each model so as to make sure that the models behave differently at high densities. The models have different evolution patterns of nuclear properties with respect to density, even if fitted to the same saturation properties. In Ref. [29] similar discussions have been carried out with the modified QMC (MQMC) model that has a density-dependent bag constant. Instead of MQMC, here we focus on the CQMC model, confirming the results for the other models, i.e., QHD2, QMC1, and QMC2.

The rest of this paper is organized as follows: Section II briefly introduces the model framework used to describe nuclear systems. Section III presents numerical results concerning static properties of finite nuclei and nuclear matter. The calculated cross sections of $(e, e'p)$ reactions are also discussed. Finally, conclusions are drawn in Sec. IV.

II. FORMALISM

A. Chiral quark-meson coupling model

The details of the derivation of the CQMC model may be found in Ref. [21]. The CQMC model can be briefly introduced in the Lagrangian density that contains the fields for quarks (ψ), isoscalar scalar (σ) and vector (ω_μ) and isovector

vector ($\boldsymbol{b}_\mu$) mesons:

$$\mathcal{L}_{\text{CQMC}} = \mathcal{L}_{\text{CBM}} + \tfrac{1}{2}\big(\partial_\mu \sigma \partial^\mu \sigma - m_\sigma^2 \sigma^2\big) - \tfrac{1}{4}W_{\mu\nu}W^{\mu\nu}$$
$$+ \tfrac{1}{2}m_\omega^2 \omega_\mu \omega^\mu - \tfrac{1}{4}\boldsymbol{G}_{\mu\nu} \cdot \boldsymbol{G}^{\mu\nu} + \tfrac{1}{2}m_\rho^2 \boldsymbol{b}_\mu \cdot \boldsymbol{b}^\mu$$
$$+ \bar{\psi}\big(g_\sigma^q \sigma - g_\omega^q \omega - \tfrac{1}{2}g_\rho^q \boldsymbol{\tau} \cdot \boldsymbol{b}\big)\psi\, \theta_V,$$

$$\mathcal{L}_{\text{CBM}} = \mathcal{L}_{\text{bag}} + \mathcal{L}_\pi + \mathcal{L}_g + \mathcal{L}_{\text{int}},$$

$$\mathcal{L}_{\text{bag}} = [\bar{\psi}(i\slashed{\partial} - m_q)\psi - B]\theta_V - \tfrac{1}{2}\bar{\psi}\psi\,\delta_S, \quad (1)$$

where $W_{\mu\nu}$ and $\boldsymbol{G}_{\mu\nu}$ indicate the field strength tensors of ω_μ and $\boldsymbol{b}_\mu$ fields, respectively. The interactions between the quarks and mesons are restricted to occur inside the bag by θ_V, the step function. The Lagrangian density of the volume-coupling version of the cloudy bag model (CBM) [30], $\mathcal{L}_{\text{CBM}}$, consists of the simple bag ($\mathcal{L}_{\text{bag}}$), free pion field ($\mathcal{L}_\pi$), gluon kinetic energy ($\mathcal{L}_g$), and quark-pion and -gluon interactions ($\mathcal{L}_{\text{int}}$). In this model, the effective nucleon mass in the external fields can be obtained as the total energy of the bag and the energy shift due to pion and gluon;

$$M_N^* = \frac{3\Omega - z}{R^*} + \frac{4}{3}\pi B R^{*3} + E_\pi + E_g \quad (2)$$

with

$$\Omega = \sqrt{x^{*2} + (R^* m_q^*)^2}. \quad (3)$$

The bag constant B and the parameter for the zero-point motion z are fitted to reproduce the mass of a free nucleon. The energy of a quark Ω is given in terms of the momentum of a quark in a bag, x^*, the bag radius R^*, and the effective mass of the quark, $m_q^* = m_q - g_\sigma^q \sigma$. The bag radius is determined by the equilibrium condition for the bag in medium. The quantity x^* is inherently given from the boundary condition at the bag surface, $j_0(x) = \beta_q j_1(x)$, where $\beta_q = \sqrt{(\Omega - R^* m_q^*)/(\Omega + R^* m_q^*)}$.

B. Description of finite nuclei

The effective Lagrangian density for spherical nuclei in nucleon (N) degrees of freedom can be given as

$$\mathcal{L} = \bar{N}\Big[i\slashed{\partial} - M_N^* - g_\omega \omega - \frac{g_\rho}{2}\boldsymbol{\tau} \cdot \boldsymbol{b} - \frac{e}{2}(1 + \tau_3)\slashed{A}\Big]N$$
$$+ \frac{1}{2}\big(\partial_\mu \sigma \partial^\mu \sigma - m_\sigma^2 \sigma^2\big) - U_\sigma - \frac{1}{4}W_{\mu\nu}W^{\mu\nu} + \frac{1}{2}m_\omega^2 \omega_\mu \omega^\mu$$
$$- \frac{1}{4}\boldsymbol{G}_{\mu\nu} \cdot \boldsymbol{G}^{\mu\nu} + \frac{1}{2}m_\rho^2 \boldsymbol{b}_\mu \cdot \boldsymbol{b}^\mu - \frac{1}{4}F_{\mu\nu}F^{\mu\nu}, \quad (4)$$

where the field strength tensor $F_{\mu\nu}$ of electromagnetic field A_μ is appended. The effective nucleon mass is defined by

$$M_N^* = M_N - g_\sigma(\sigma)\sigma \quad (5)$$

with

$$g_\sigma(\sigma) = g_\sigma b_N\Big[1 - \frac{a_N}{2}(g_\sigma \sigma)\Big]. \quad (6)$$

The σ-N coupling as a function of σ field, Eq. (6), is parametrized with two parameters, a_N and b_N, which are determined in order to reproduce the effective mass in a quark-level calculation like Eq. (2). Therefore a_N and b_N are
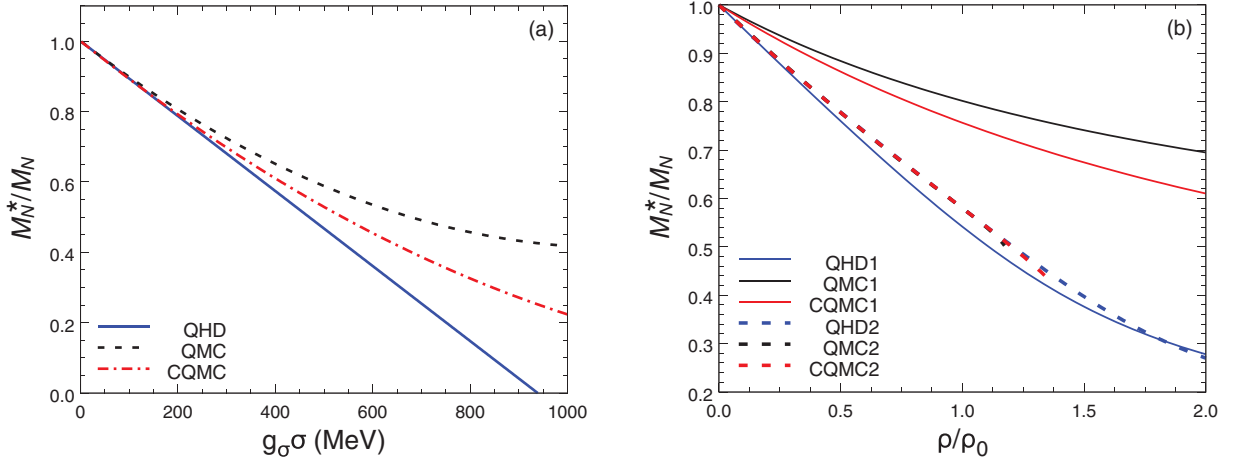
FIG. 1. Effective nucleon mass ratio as a function (a) of scalar field and (b) of density. In the case of (a), there is no difference between the models 1 and 2 because $M_N^*(g_\sigma \sigma)$ can be identified only by the set of a_N and b_N. In contrast, in (b) the models 1 and 2 are distinguished because the existence of the nonlinear self-interaction terms affects the relation between σ field and density.

the important parameters to infer the subnucleonic structure described by each model. The effective mass ratio described in each model is shown in Fig. 1. The main distinction between the models (QHD, QMC, and CQMC) at the level of Eq. (4) arises only from the different sets of a_N and b_N. For example, once we set $a_N = 0$ and $b_N = 1$, the σ-N coupling, $g_\sigma(\sigma)$, becomes consistent with the constant g_σ in QHD.

Introducing the specific form of the nonlinear scalar self-interactions,

$$U_\sigma = \tfrac{1}{3} g_2 \sigma^3 + \tfrac{1}{4} g_3 \sigma^4, \tag{7}$$

the effective Lagrangian density, Eq. (4), has five couplings (g_σ, g_ω, g_ρ, g_2, and g_3) to be determined. For the models denoted by 1, the nonlinear σ couplings, g_2 and g_3, are set to be zero, otherwise the couplings are fitted to three nuclear saturation properties. We use the symmetry energy of $E_{\text{sym}} = 32.5$ MeV and the binding energy per nucleon $B/A = -15.7$ MeV at the saturation density $\rho_0 = 0.15$ fm^{-3}. For the models 2, we need to fix two more saturation properties in order for g_2 and g_3 to be determined: the incompressibility $K = 260$ MeV and the effective nucleon mass ratio $M_N^*/M_N = 0.58$. It has been shown that, for models without isoscalar

tensor coupling, a value of M_N^*/M_N in between 0.58 to 0.64 at saturation density is required in order to reproduce the empirical values of spin-orbit splitting in nuclei [31]. Here we take $M_N^*/M_N = 0.58$ with which the models 2 yield better agreement with the experimental data in the single-particle levels. The mass of the scalar meson, m_σ, is also a parameter, typically in the range of 400–550 MeV [32], and has been adjusted to find the rms charge radius of ^{40}Ca (3.48 fm). Consequently the QMC2 and CQMC2 have been required to have scalar masses much larger than the typical values. The parameter sets we used for each model are listed in Table I. The QHD1 corresponds to the model in Ref. [3] although the couplings in Table I differ from those in Ref. [3] because of the up-to-date saturation properties.

III. NUMERICAL RESULTS

A. Finite nuclei

Figure 2 shows the nuclear and charge densities of ^{40}Ca compared with the empirical distributions. The model difference beyond $r > 3$ fm is compensated by the choice of scalar mass. For the interior region, it remains significant, being the

TABLE I. Coupling constants and saturation properties.

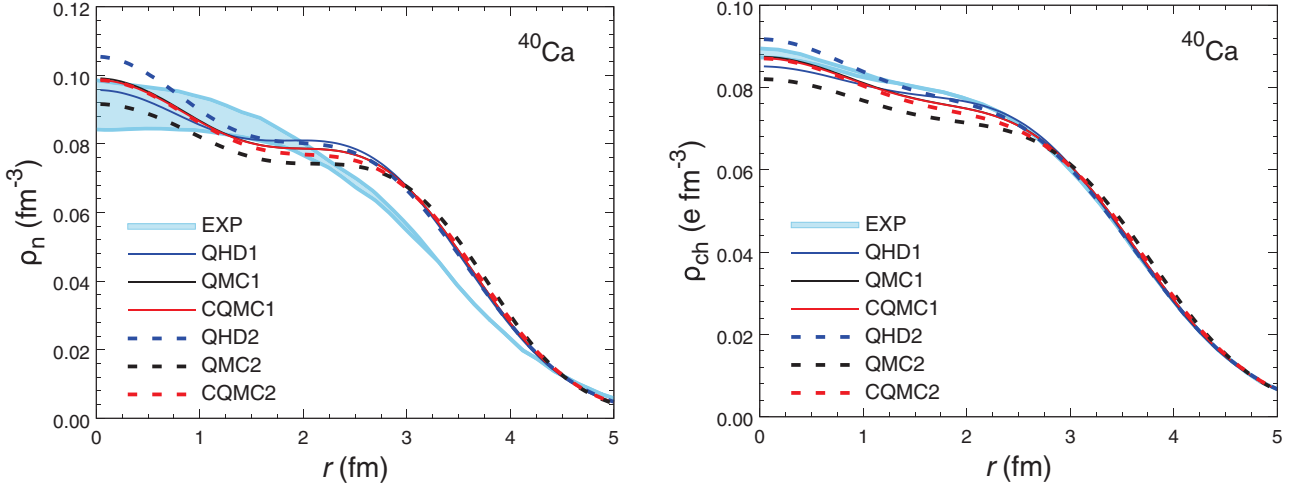|	QHD1	QMC1	CQMC1	QHD2	QMC2	CQMC2
g_σ	10.326	6.859	7.459	10.331	14.413	11.835
g_ω	13.708	8.245	9.450	13.065	13.065	13.065
g_ρ	7.348	8.752	8.578	7.635	7.635	7.635
g_2	0	0	0	10.400	−46.912	−12.251
g_3	0	0	0	−30.866	19.151	−20.042
a_N	0	0.179	0.118	0	0.179	0.118
b_N	1	1	1.04	1	1	1.04
m_σ (MeV)	515.91	455.67	482.56	509.75	734.40	619.52
K (MeV)	545	280	302	260	260	260
M_N^*/M_N	0.54	0.80	0.76	0.58	0.58	0.58
L	107.97	88.68	90.67	105.83	105.83	105.83

FIG. 2. Nuclear and charge densities for ^{40}Ca compared with the empirical data [33,34].

largest in the central region. The CQMC models well describe the empirical charge density in the central region while the QMC2 has a large depression of the central densities. The other nuclei have similar tendencies in model difference.

Table II displays the calculated values of the binding energy (E/A) and charge radius (r_c) for the stable nuclei of concern. There is found no significant difference between the models for the charge radius. The models 2 provide reasonable binding energies compared to the empirical data. The QMC1 and CQMC1 models lead to (less accurate but still) fair descriptions of the bulk properties of nuclei. The exceptional failure of QHD1, particularly in the binding energies exhibited in Table II, could be interpreted as being caused by the physically preposterous values of the saturation properties, e.g., $K > 500$ MeV as shown in Table I. If the nuclear saturation properties that a model reproduces are far from the empirical, it is hard for the model to describe the finite nuclei properly.

The models 2 have the vector couplings identical to each other and hold in common the empirical values of saturation properties. The difference of the models 2 is on the basis of their scalar potential, which is related to the surface properties of the nuclei. The model difference in the bulk properties of nuclei tends to be reduced for the heavier nuclei. If one wants to figure out how reliable or applicable the models are to finite nuclei, one needs to study the single-particle spectra.

The single-particle energy levels for ^{40}Ca are presented in Fig. 3. The QMC1 and CQMC1 provide insufficient binding energy to reproduce the single-particle levels of the nuclei, as can be seen in Table II and Fig. 3. For the QHD2 and CQMC2 models, the states $2s_{1/2}$ and $1d_{3/2}$ are arranged in the correct order of experimental data. This ordering is sensitively dependent on the value of the effective nucleon mass at saturation density. The QMC2 model has no chance to make the order of the states correct for any possibility of $0.58 \leqslant M_N^*/M_N \leqslant 0.64$. The calculation of $(e, e'p)$ scattering cross section is influenced by model difference in the single-particle state energy. In Sec. III C, we are going to discuss it in comparison with the experimental data for spherical nuclei.

The static properties of finite nuclei evaluated in each model are more sensitive to the nuclear saturation properties than microscopic details of the models since they are parametrized. When it comes to the chiral symmetry as an example, none of nuclear bulk properties directly manifests such a fundamental property of QCD. The nuclear saturation properties in each model are determined or input by hand regardless of whether the quark-level Lagrangian is chirally symmetric or not. Therefore, QHD2, having the nonlinear scalar self-interaction, despite the pointlike nucleons in it, was able to show a remarkable improvement compared with QHD1 for finite nuclei.

TABLE II. Ground-state properties for spherical nuclei: Binding energy per nucleon, E/A, in MeV and charge radius, r_c, in fm. The experimental data are taken from Refs. [36,37].

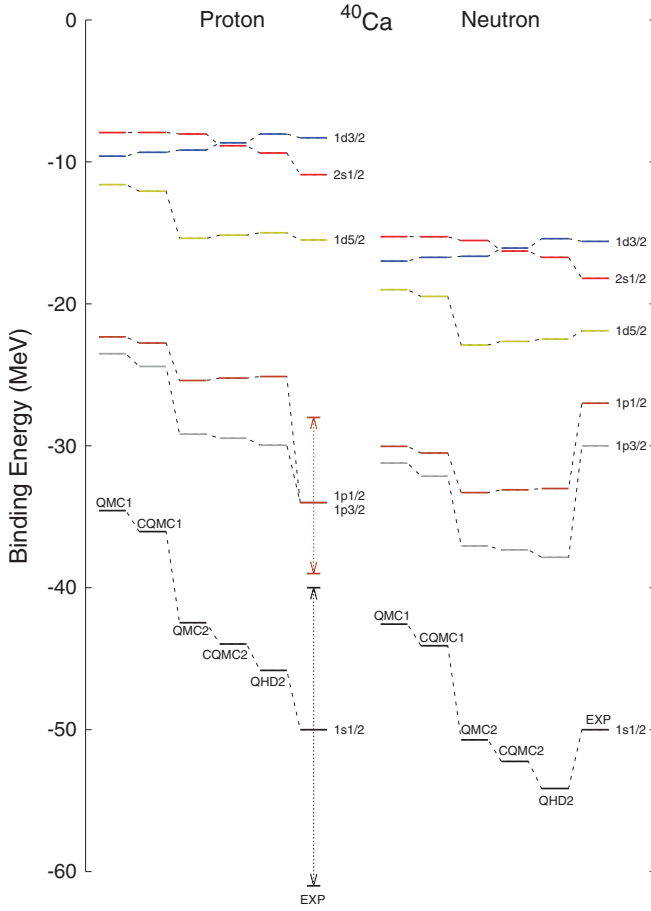|	^{16}O		^{40}Ca		^{48}Ca		^{90}Zr		^{208}Pb	
	E/A	r_c	E/A	r_c	E/A	r_c	E/A	r_c	E/A	r_c
QHD1	−5.44	2.76	−6.36	3.48	−6.74	3.47	−6.96	4.26	−6.53	5.45
QMC1	−7.15	2.76	−7.73	3.48	−7.59	3.53	−7.77	4.30	−7.08	5.56
CQMC1	−7.04	2.76	−7.63	3.48	−7.54	3.52	−7.72	4.30	−7.04	5.54
QHD2	−7.61	2.74	−8.05	3.48	−8.25	3.47	−8.24	4.27	−7.52	5.51
QMC2	−8.58	2.73	−8.67	3.48	−8.81	3.52	−8.65	4.29	−7.77	5.54
CQMC2	−8.04	2.74	−8.37	3.48	−8.47	3.50	−8.43	4.28	−7.67	5.53
Expt.	−7.98	2.73	−8.45	3.48	−8.57	3.47	−8.66	4.27	−7.86	5.50

FIG. 3. Single particle energy spectra of ^{40}Ca. The experimental data are taken from Ref. [35].

B. Nuclear matter

Contrary to the case of finite nuclei, the CQMC perspectives have turned out to influence the nuclear matter properties [22,24,25]. In Fig. 4(a), we present the equation of state (EoS)
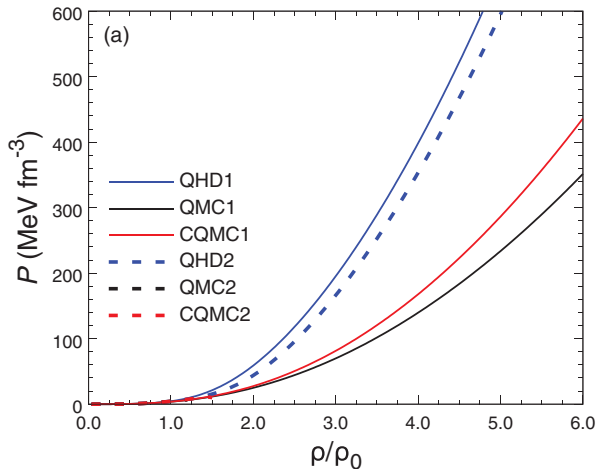
for infinite nuclear matter by using the same models as in the previous section. The CQMC model makes the EoS stiff in comparison with the QMC model so that it raises the mass of a neutron star as shown in Fig. 4(b).

The characteristic of each model becomes pronounced at higher densities rather than near-saturation densities. The evolution of nuclear properties with respect to density depends on the models even though the model parameters are fitted to the same saturation properties. In the context of the effective nucleon mass, as shown in Fig. 1, the models 1 reveal a large discrepancy already at low density regions and it becomes larger at higher densities. The models 2 have almost identical behavior at near-saturation densities. But unfortunately the QMC2 and CQMC2 are not suitable for the supradense systems because the equation of motion for the scalar meson has no solution at high density regions. From the Lagrangian the scalar field equation is written as

$$m_\sigma^2 \sigma + g_2 \sigma^2 + g_3 \sigma^3 = C_N(\sigma) g_\sigma \rho_s, \qquad (8)$$

where ρ_s indicates the scalar density and $C_N(\sigma) = b_N[1 - a_N(g_\sigma \sigma)]$. With the function $f(\sigma)$ defined as

$$f(\sigma) \equiv \frac{g_\sigma}{m_\sigma^2}(C_N(\sigma) g_\sigma \rho_s - g_2 \sigma^2 - g_3 \sigma^3) - g_\sigma \sigma, \quad (9)$$

it is demonstrated in Fig. 5 that the solution of $f(\sigma) = 0$ cannot be found at about $\rho = 0.19$ fm^{-3} for QMC2 and at about $\rho = 0.24$ fm^{-3} for the CQMC2 model, respectively. This does not happen for the models 1 because $f(\sigma)$ with $g_2 = g_3 = 0$ is monotonic. The conventional nonlinear scalar fields used here for the models 2 makes the field equation asymptotically unphysical and the solution of $f(\sigma) = 0$ double valued [38]. The extended parametrizations of the nonlinearity can help the scalar field behave monotonically [38,39] and may improve the (C)QMC2 models, giving a solution at high densities.

C. Electron scattering off nuclei

This section is devoted to discussing the one-proton knock-out $(e, e'p)$ reactions, for which the quasielastic cross section
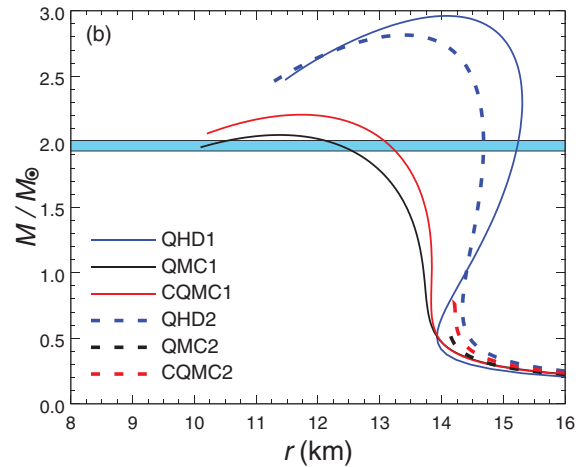

FIG. 4. (a) The equation of state and (b) the mass of a neutron star as a function of radius. The shaded region stands for the observational constraint of a two-solar-mass neutron star (PSR J1611−2230) [26–28].
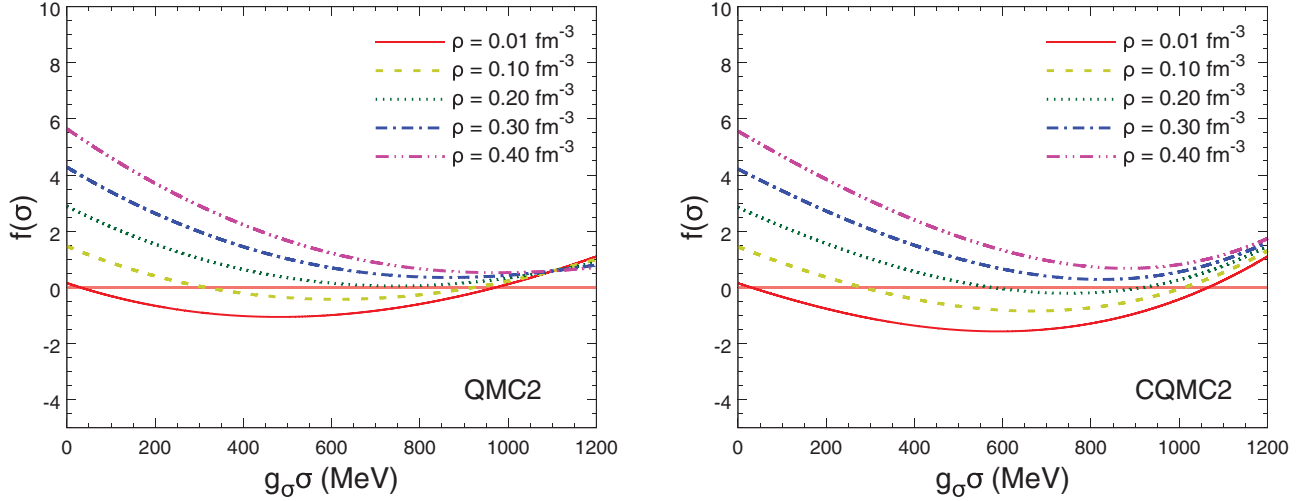
FIG. 5. Discriminant of Eq. (9) at various baryon densities.

is a useful tool for studying the single-particle properties of the target nucleus. Using the kinematic variables depicted in Fig. 6, the cross section can be decomposed into five response functions:

$$\frac{d^3\sigma}{dE_f \, d\Omega_f \, d\Omega_p} = \frac{pE_p}{(2\pi)^3}\, \sigma_{\rm M}[v_{\rm L}R_{\rm L} + v_{\rm T}R_{\rm T} + \cos 2\phi_p \, v_{\rm TT}R_{\rm TT}$$
$$+ \cos\phi_p \, v_{\rm LT}R_{\rm LT} + h\sin\phi_p \, v_{\rm LT'}R_{\rm LT'}], \quad (10)$$

where the Mott cross section is given by

$$\sigma_{\rm M} = \frac{\alpha^2}{4E_i^2} \frac{\cos^2(\theta_e/2)}{\sin^4(\theta_e/2)}. \quad (11)$$

In the right-hand side of Eq. (10), $R_{\rm L/T}$ are referred to as the longitudinal/transverse response functions, and $R_{\rm LT/TT}$ describe longitudinal-transverse/transverse-transverse interferences, respectively. The fifth one, $R_{\rm LT'}$, indicates the

polarized longitudinal-transverse interference, which is directly proportional to the electron beam asymmetry. These functions, which contain essential information on the nucleons inside the nucleus, can be obtained from the components of the nuclear tensor $W_{\mu\nu}$:

$$R_{\rm L} = W_{00}, \qquad R_{\rm T} = W_{11} + W_{22},$$
$$R_{\rm TT} = \frac{1}{\cos 2\phi_p}(W_{11} - W_{22}),$$
$$R_{\rm LT} = \frac{1}{\cos \phi_p}(W_{01} - W_{10}),$$
$$R_{\rm LT'} = \frac{-i}{\sin \phi_p}(W_{02} + W_{20}). \quad (12)$$

For an explicit calculation of $W_{\mu\nu}$, we exploit the nuclear models employed in the previous sections (in particular QHD1, QHD2, QMC1, and CQMC1), keeping in mind that those models have a slight difference between their single-particle state energies, as shown in Fig. 3. The electron kinematic factors in Eq. (10) are given in terms of the four-momentum transfer, $q = (\omega, \mathbf{q})$, and the electron scattering angle θ_e:

$$v_{\rm L} = \frac{q^4}{\mathbf{q}^4}, \qquad v_{\rm T} = \tan^2\frac{\theta_e}{2} - \frac{q^2}{2\mathbf{q}^2},$$
$$v_{\rm TT} = -\frac{q^2}{2\mathbf{q}^2},$$
$$v_{\rm LT} = -\frac{q^2}{\mathbf{q}^2}\left(\tan^2\frac{\theta_e}{2} - \frac{q^2}{2\mathbf{q}^2}\right),$$
$$v_{\rm LT'} = -\frac{q^2}{\mathbf{q}^2}\tan^2\frac{\theta_e}{2}. \quad (13)$$

For more technical details, such as the treatment of the Coulomb distortion of electrons, we follow Refs. [40–44].

As is commonly done in the analysis of the quasielastic $(e, e'p)$ reaction, the data are displayed with the reduced cross section, ρ_m, which is defined as the measured cross section
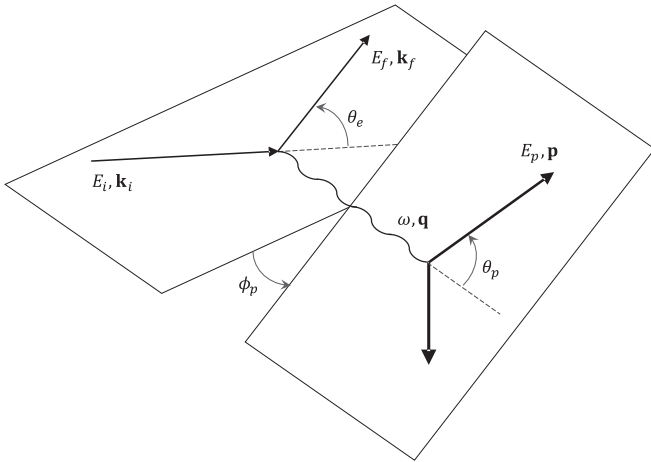

FIG. 6. Kinematics for the one-proton knockout $(e, e'p)$ reaction: energy and momentum of incident electron $(E_i, \mathbf{k}_i)$, scattered electron $(E_f, \mathbf{k}_f)$, virtual photon $(\omega, \mathbf{q})$ and knocked out proton $(E_p, \mathbf{p})$. The azimuthal angle ϕ_p is defined as the angle between the reaction plane and the scattering plane.

divided by the kinematic factors:

$$\rho_m(\mathbf{p}_m) = \frac{1}{p \, E_p \, \sigma_{ep}} \frac{d^3\sigma}{dE_f \, d\Omega_f \, d\Omega_p}, \qquad (14)$$

where the missing momentum is defined by $\mathbf{p}_m = \mathbf{p} - \mathbf{q}$. The reduced cross section in the plane-wave approximation provides information about the nucleon spectral function: the probability of ejecting a nucleon from the target nucleus with momentum and binding energy. The momentum distribution of the spectral function is essentially the squared Fourier transform of the overlap wave function between the ground state of the target nucleus and the final state of the residual nucleus. The overlap wave function is closely related to the bound state wave function of the ejected nucleon. In order to calculate Eq. (14), it is required to select a model for the off-shell electron-proton cross section, σ_{ep}, since it is not uniquely defined. We take the so-called CC1 prescription for σ_{ep} [45], which is widely used to calculate the cross sections. To take the final state interaction into account, the wave functions of the knocked-out proton are derived using a relativistic optical potential fitted to proton-nucleus elastic scattering [46].

To compare the calculated cross sections with experimental data, two different kinematics are considered. On one hand, parallel kinematics is defined by $\theta_p = 0$, and thus $\mathbf{p}_m$ is parallel to $\mathbf{q}$. The parallel kinematics is used to observe protons ejected along the momentum transfer $\mathbf{q}$. This can be realized by selecting both the incoming and the outgoing electron energies and then determining the momentum transfer direction for each scattering angle. On the other hand, perpendicular kinematics (the so-called $\omega - q$ constant kinematics) is the kinematics in which $|\mathbf{p}|$ is fixed to be equal to $|\mathbf{q}|$ while varying θ_p within a small range by fixing the electron kinematics and then measuring the knocked-out proton angular distribution. In such cases $\mathbf{p}_m$ is nearly perpendicular to $\mathbf{q}$. In the parallel kinematics, the three interference terms in Eq. (10) disappear by integrating over the azimuthal angle ϕ_p, while, in the perpendicular kinematics, all the terms remain except the fifth term which sums to zero for unpolarized incident electron beam.

Extraction of the spectral function as well as the response functions using the kinematics in the $(e, e'p)$ reaction is very useful for quantitatively understanding the recent the muon-neutrino (ν_μ) scattering off ^{12}C at the MiniBooNE [47], although the axial part absent from the $(e, e'p)$ reaction is reported to dominate the charged current quasielastic scattering by the kaon decay at rest (KDAR) ν_μ [48].

In Fig. 7, the reduced cross sections of $^{40}Ca(e, e'p)$ are plotted as a function of the missing momentum. In parallel kinematics, all the models reproduce in fairly good agreement the experimental data [49], using the spectroscopic factors of 0.75 for the $2s_{1/2}$ shell and of 0.8 for the $1d_{3/2}$ shell [50–52]. None of the nuclear structure models tried makes remarkable improvement to the cross section. Indeed, the curves for QHD2, QMC1, and CQMC1 in parallel kinematics are so close that they are hardly distinguished. Their difference from QHD1 is also insignificant (at most less than 15 %).

Around the peaks, the result of the QHD1 is the largest of other calculations at both $2s_{1/2}$ and $1d_{3/2}$ orbits in the parallel

kinematics. In the perpendicular kinematics, the result of the QMC1 is the largest at the $2s_{1/2}$ state but that of QHD1 is the biggest at the $1d_{3/2}$ state around the peaks. In particular, the results at the $1d_{3/2}$ orbit show the similar behavior in both kinematics, but those of the $2s_{1/2}$ orbit demonstrate different behavior. The differences between curves are at most about 15 %. From these results, one may realize that the magnitudes of the reduced cross sections for different orbits are dependent on the nuclear models although the shapes are the same. The differences between the curves are similar to those of both kinematics except the case of the $2s_{1/2}$ orbit in the perpendicular kinematics.

In perpendicular kinematics, the model dependence of the reduced cross section is akin to that in parallel kinematics in the sense that there is rarely a meaningful distinction between the models. Although there remains room for discussion as to some details (for instance what makes, only in the lower-left panel of Fig. 7, the agreement of QMC1 with the experimental data less favorable), more in-depth investigation for detailed analysis is left for future work. Here we would like to stress that the reduced cross sections shown in Fig. 7 do not directly manifest the effect of models for the nucleon structure. This went against our naive expectations that the model difference in single-particle state energies in Fig. 3 may affect the kinematics of the knocked-out proton from a given state. Actually we did the same calculations for other spherical nuclei, e.g., ^{16}O and ^{208}Pb, but omitted to present the results for them because there is nothing different to be interpreted.

IV. SUMMARY AND CONCLUSION

In this work we have revisited the ground-state properties of spherical nuclei to explore the difference of the various QHD-type models: QHD, QMC, and CQMC. In particular, we focused on the CQMC model, which has not been applied to finite nuclei before. The models are divided into two types, denoted by 1 and 2, according to the absence and presence of the nonlinear scalar self-interactions. The coupling parameters are determined in order to reproduce the nuclear saturation properties. The nonlinear scalar self-interactions play an important role in such a way that they provide enough number of parameters to fix nuclear saturation properties to their empirical values. For the models 1 without the nonlinear self-interactions, the incompressibility and the effective nucleon mass at saturation are determined far from the empirical values. The models 2 are useful to verify the model difference because they have the empirical saturation value of the effective mass and also the same vector couplings.

Table II shows that the QMC2 and CQMC2 models, which can reproduce the empirical saturation properties, lead to reasonably fair results for the binding energies and charge radii of spherical nuclei. The QMC1 and CQMC1 have too small scalar field to reproduce the empirical binding energies and single-particle spectra. The CQMC2 is relatively advantageous for describing the ordering of the single-particle levels, $2s_{1/2}$ and $1d_{3/2}$, and the charge density in the interior region, in comparison with QMC2 model. We do not mention any interpretation in direct connection to modeling in the quark-level Lagrangian since the QMC and CQMC
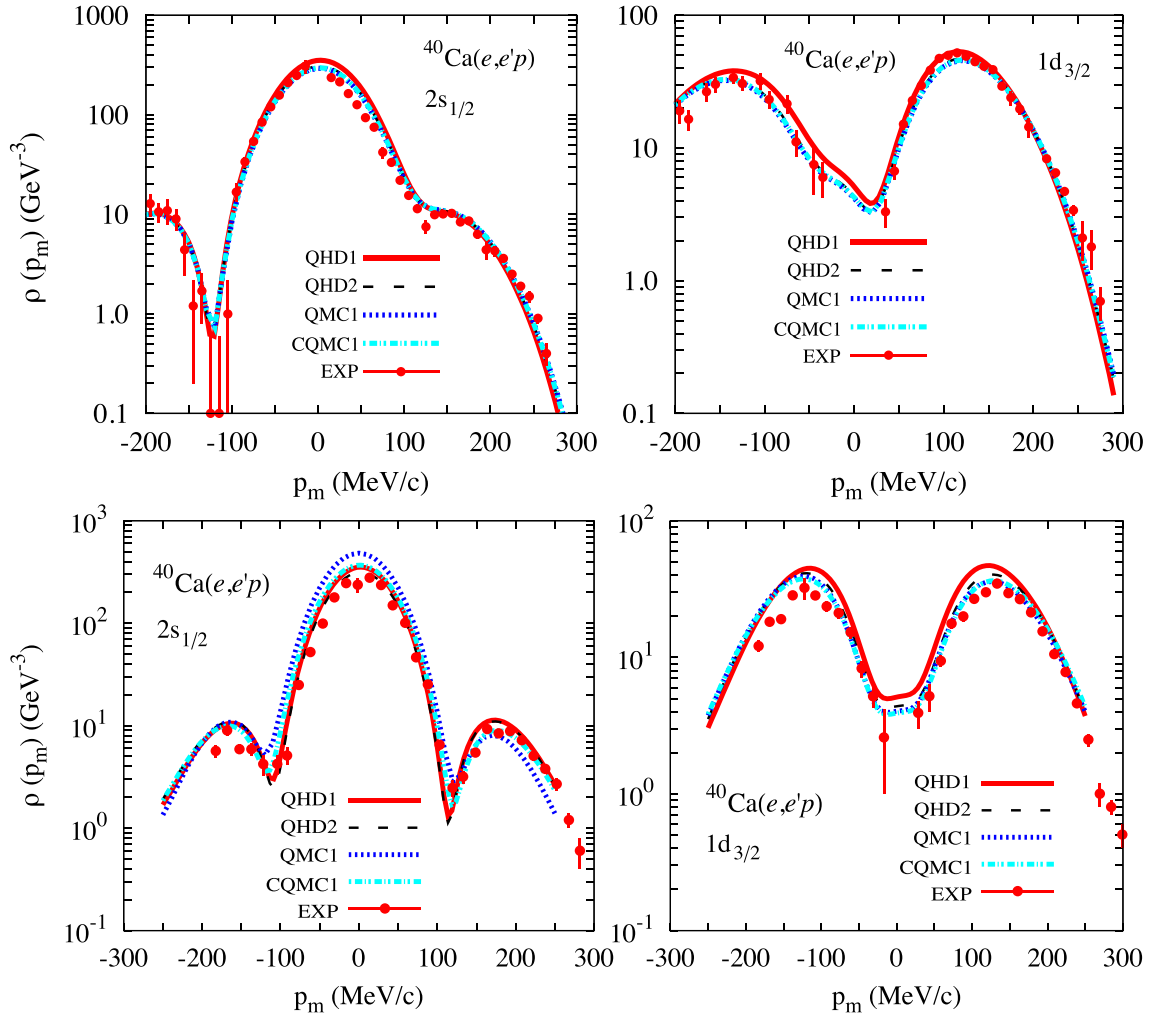
FIG. 7. Reduced cross section for the knocked-out proton from $2s_{1/2}$ (left panels) and $1d_{3/2}$ (right panels) of ^{40}Ca in parallel (upper panels) and perpendicular (lower panels) kinematics. The experimental data are taken from NIKHEF [49] at kinematic setting $E_i = 375$ MeV, $\omega = 100$ MeV, and $\theta_e = 83°$.

models used here are all parametrized; the information of subnucleonic structure described in each model is encoded into the effective nucleon mass. However, the difference between the predictions of QMC2 and CQMC2 is surely attributable to the rigorous description of the fundamentals of QCD.

The models have been examined for nuclear properties at higher densities where the repulsive core of NN interaction becomes more significant. The QMC1 and CQMC1, which have weakly repulsive core, make the maximum mass of neutron star small. The contribution of nonlinear terms in QHD2 does not dramatically change the EoS compared to the QHD1, as seen in Fig. 4. The QMC2 and CQMC2 are restricted in applicability because their meson field equations no longer have solutions above $\rho/\rho_0 \approx 1.4$. The models have been examined for nuclear properties at higher densities where the repulsive core of NN interaction becomes more significant. The QMC1 and CQMC1, which have weakly repulsive core, make the maximum mass of a neutron star small. The contribution of nonlinear terms in QHD2 does not dramatically change the EoS compared to the QHD1, as seen in Fig. 4. The QMC2 and

CQMC2 are restricted in applicability because their meson field equations no longer have solutions above $\rho/\rho_0 \approx 1.4$.

We also have done the calculation of quasielastic ^{40}Ca$(e, e'p)$ cross section using the theoretical framework based on the distorted-wave impulse approximation (DWIA), where the final-state interaction and the Coulomb distortion of electrons have been included. As several nuclear models are used to extract the bound-state wave functions, it can be tested if and how the model difference in the single-particle state energies could contribute to the spectral function of knocked-out proton. In Fig. 7, it is not easy to discern a difference between the effects of the models which incorporate the influence of the nucleon structure, e.g., QHD2, QMC1, and CQMC1. Calculations can be further developed by considering correlation effects, such as pairings. Explicit treatment of the residual interaction in the Hartree-Fock-Bogoliubov (HFB) approximation for each model could support more consistent spectroscopic factors for the possible smearing of the energy levels around the Fermi surface. Besides, kinematically taking into account meson exchange contributions, which involve transverse excitations, could also be helpful to improve the

agreement with the experiment. They are interesting and important contributions, but are beyond the scope of the present work.

ACKNOWLEDGMENTS

[1] J. D. Walecka, Ann. Phys. (NY) **83**, 491 (1974).

[2] S. A. Chin, Ann. Phys. (NY) **108**, 301 (1977).

[3] C. J. Horowitz and B. D. Serot, Nucl. Phys. A **368**, 503 (1981).

[4] C. J. Horowitz and B. D. Serot, Nucl. Phys. A **399**, 529 (1983).

[5] B. D. Serot and J. D. Walecka, in *Advances in Nuclear Physics*, edited by J. W. Negele and E. Vogt, Vol. 16 (Plenum Press, New York, 1986).

[6] Y. K. Gambhir, P. Ring, and A. Thimet, Ann. Phys. (NY) **198**, 132 (1990).

[7] B. D. Serot and J. D. Walecka, Int. J. Mod. Phys. E **6**, 515 (1997).

[8] P. Navratil, J. P. Vary, and B. R. Barrett, Phys. Rev. Lett. **84**, 5728 (2000).

[9] B. R. Barrett, P. Navratil, and J. P. Vary, Prog. Part. Nucl. Phys. **69**, 131 (2013).

[10] R. B. Wiringa and S. C. Pieper, Phys. Rev. Lett. **89**, 182501 (2002).

[11] S. C. Pieper, R. B. Wiringa, and J. Carlson, Phys. Rev. C **70**, 054325 (2004).

[12] G. Hagen, M. Hjorth-Jensen, G. R. Jansen, R. Machleidt, and T. Papenbrock, Phys. Rev. Lett. **109**, 032502 (2012).

[13] G. Hagen *et al.*, Nat. Phys. **12**, 186 (2015).

[14] K. Tsukiyama, S. K. Bogner, and A. Schwenk, Phys. Rev. Lett. **106**, 222502 (2011).

[15] S. K. Bogner, H. Hergert, J. D. Holt, A. Schwenk, S. Binder, A. Calci, J. Langhammer, and R. Roth, Phys. Rev. Lett. **113**, 142501 (2014).

[16] P. A. M. Guichon, Phys. Lett. B **200**, 235 (1988).

[17] K. Saito and A. W. Thomas, Phys. Lett. B **327**, 9 (1994).

[18] K. Saito, K. Tsushima, and A. W. Thomas, Nucl. Phys. A **609**, 339 (1996).

[19] K. Saito, K. Tsushima, and A. W. Thomas, Phys. Rev. C **55**, 2637 (1997).

[20] K. Saito, K. Tsushima, and A. W. Thomas, Prog. Part. Nucl. Phys. **58**, 1 (2007).

[21] S. Nagai, T. Miyatsu, K. Saito, and K. Tsushima, Phys. Lett. B **666**, 239 (2008).

[22] T. Miyatsu and K. Saito, Few Body Syst. **54**, 1591 (2013).

[23] T. Miyatsu, M. K. Cheoun, and K. Saito, Astrophys. J. **813**, 135 (2015).

[24] T. Miyatsu, T. Katayama, and K. Saito, Phys. Lett. B **709**, 242 (2012)

[25] T. Katayama, T. Miyatsu, and K. Saito, Astrophys. J. Suppl. **203**, 22 (2012).

[26] P. Demorest, T. Pennucci, S. Ransom, M. Roberts, and J. Hessels, Nature (London) **467**, 1081 (2010).

[27] J. Antoniadis *et al.*, Science **340**, 1233232 (2013).

[28] M. Linares, T. Shahbaz, and J. Casares, Astrophys. J. **859**, 54 (2018).

[29] H. Müller and B. K. Jennings, Nucl. Phys. A **640**, 55 (1998).

[30] A. W. Thomas, J. Phys. G **7**, L283 (1981).

[31] R. J. Furnstahl, J. J. Rusnak, and B. D. Serot, Nucl. Phys. A **632**, 607 (1998).

[32] M. Tanabashi *et al.* (Particle Data Group), Phys. Rev. D **98**, 030001 (2018).

[33] I. Sick *et al.*, Phys. Lett. B **88**, 245 (1979).

[34] L. Ray and P. E. Hodgson, Phys. Rev. C **20**, 2403 (1979).

[35] X. Campi and D. W. Sprung, Nucl. Phys. A **194**, 401 (1972).

[36] M. Wang *et al.*, Chin. Phys. C **36**, 1603 (2012).

[37] I. Angeli and K. P. Marinova, At. Data Nucl. Data Tables **99**, 69 (2013).

[38] P. G. Reinhard, Z. Phys. A **329**, 257 (1988).

[39] H. Fujii, T. Maruyama, T. Muto, and T. Tatsumi, Nucl. Phys. A **597**, 645 (1996).

[40] K. S. Kim, L. E. Wright, Y. Jin, and D. W. Kosik, Phys. Rev. C **54**, 2515 (1996).

[41] K. S. Kim and L. E. Wright, Phys. Rev. C **56**, 302 (1997).

[42] K. S. Kim and L. E. Wright, Phys. Rev. C **60**, 067604 (1999).

[43] K. S. Kim, L. E. Wright, and D. A. Resler, Phys. Rev. C **64**, 044607 (2001).

[44] K. S. Kim and L. E. Wright, Phys. Rev. C **72**, 064607 (2005).

[45] T. De Forest, Nucl. Phys. A **392**, 232 (1983).

[46] E. D. Cooper, S. Hama, B. C. Clark, and R. L. Mercer, Phys. Rev. C **47**, 297 (1993).

[47] A. A. Aguilar-Arevalo *et al.* (MiniBooNE Collaboration), Phys. Rev. Lett. **120**, 141802 (2018).

[48] A. Nikolakopoulos, V. Pandey, J. Spitz, and N. Jachowicz, Phys. Rev. C **103**, 064603 (2021).

[49] G. J. Kramer *et al.*, Phys. Lett. B **227**, 199 (1989).

[50] Y. Jin, D. S. Onley, and L. E. Wright, Phys. Rev. C **45**, 1311 (1992).

[51] Y. Jin, D. S. Onley, and L. E. Wright, Phys. Rev. C **45**, 1333 (1992).

[52] Y. Jin, D. S. Onley, and L. E. Wright, Phys. Rev. C **50**, 168 (1994).